



X-Ray Properties of Radio-selected Dual Active Galactic Nuclei

Arran C. Gross¹ , Hai Fu¹ , A. D. Myers², J. M. Wrobel³ , and S. G. Djorgovski⁴ ¹Department of Physics & Astronomy, The University of Iowa, 203 Van Allen Hall, Iowa City, IA 52242, USA²Department of Physics & Astronomy, University of Wyoming, Laramie, WY 82071, USA³National Radio Astronomy Observatory, P.O. Box O, 1003 Lopezville Road, Socorro, NM 87801, USA⁴California Institute of Technology, 1200 E. California Boulevard, Pasadena, CA 91125, USA

Received 2019 January 28; revised 2019 June 24; accepted 2019 July 30; published 2019 September 19

Abstract

Merger simulations predict that tidally induced gas inflows can trigger kiloparsec-scale dual active galactic nuclei (dAGN) in heavily obscured environments. Previously, with the Very Large Array, we have confirmed four dAGN with redshifts between $0.04 < z < 0.22$ and projected separations between 4.3 and 9.2 kpc in the Sloan Digital Sky Survey Stripe 82 field. Here, we present *Chandra* X-ray observations that spatially resolve these dAGN and compare their multiwavelength properties to those of single AGN from the literature. We detect X-ray emission from six of the individual merger components and obtain upper limits for the remaining two. Combined with previous radio and optical observations, we find that our dAGN have properties similar to nearby low-luminosity AGN, and they agree with the black hole fundamental plane relation well. There are three AGN-dominated X-ray sources, whose X-ray hardness-ratio derived column densities show that two are unobscured and one is obscured. The low obscured fraction suggests these dAGN are no more obscured than single AGN, in contrast to the predictions from simulations. These three sources show an apparent X-ray deficit compared to their mid-infrared continuum and optical [O III] line luminosities, suggesting higher levels of obscuration, in tension with the hardness-ratio derived column densities. Enhanced mid-infrared and [O III] luminosities from star formation may explain this deficit. There is ambiguity in the level of obscuration for the remaining five components because their hardness ratios may be affected by nonnuclear X-ray emissions, or are undetected altogether. They require further observations to be fully characterized.

Key words: galaxies: active – galaxies: interactions – galaxies: nuclei

1. Introduction

In a universe dominated by cold dark matter and dark energy, galaxies are built up from a series of major and minor mergers. Cosmological hydrodynamical simulations have shown that galaxies like our Milky Way have acquired a large ex situ component from a number of other galaxies during the cosmic history (e.g., Rodriguez-Gomez et al. 2016; Pillepich et al. 2018). Zooming in on the encounter, idealized merger simulations have predicted that gravitational torques from tidally induced stellar bars can drive large amounts of interstellar gas to the central kiloparsec on short timescales. The sudden gas inflow could dilute gas metallicity in the interstellar medium (ISM), fuel nuclear starbursts, and even trigger supermassive black hole (SMBH) accretion in the central parsec (e.g., Barnes & Hernquist 1991; Torrey et al. 2012; Capelo & Dotti 2017). As a result, simultaneous SMBH accretion could occur at the smallest, subgalactic separations ($\lesssim 10$ kpc) when the tidal force is strongest (e.g., Van Wassenhove et al. 2012; Blecha et al. 2013; Rosas-Guevara et al. 2018). Mergers in this stage would appear as kiloparsec-scale dual active galactic nuclei (dAGN) before nuclear coalescence.

The first source to be observed with signs of kiloparsec-scale dAGN activity is the radio galaxy 3C 75 (Owen et al. 1985), which shows a pair of radio jets originating from a pair of stellar nuclei separated by 7.7 kpc. More recent case studies have identified a number of kiloparsec-scale dAGN with optical and X-ray data, including LBQS 0103–2753 (Junkkarinen et al. 2001), NGC 6240 (Komossa et al. 2003), 3C 294 (Stockton et al. 2004), Arp 299 (Ballo et al. 2004), Mrk 463 (Bianchi et al. 2008), NGC 3393 (Fabbiano et al. 2011), and

Mrk 266 (Mazzarella et al. 2012). To assemble a statistical sample of dAGN with well-understood selection biases, various techniques have been developed to identify dAGN candidates and subsequently confirm them systematically. Effective candidate identification involves lower-resolution observations of larger samples: (1) double-peaked [O III] AGN in the DEEP2 Galaxy Redshift Survey (Gerke et al. 2007; Comerford et al. 2009) and in the Sloan Digital Sky Survey (SDSS; Wang et al. 2009; Liu et al. 2010; Smith et al. 2010), (2) hard-X-ray-detected nearby AGN in the Swift Burst Alert Telescope (BAT) survey (Koss et al. 2010), (3) radio AGN pairs in the Very Large Array (VLA) Stripe 82 survey (Fu et al. 2015a), (4) mid-IR-color-selected AGN in *Wide-field Infrared Survey Explorer* (WISE; Satyapal et al. 2014, 2017), (5) BPT-selected AGN in spectroscopic galaxy pairs in SDSS (Ellison et al. 2011; Liu et al. 2012; Fu et al. 2018), and (6) the *Chandra* surveys of merging galaxies (Brassington et al. 2007; Teng et al. 2012). Robust candidate confirmation requires high-resolution observations at various wavelengths, e.g., in optical and near-infrared (IR) with Keck adaptive optics imaging (Fu et al. 2011a; Rosario et al. 2011), *Hubble Space Telescope* imaging (Liu et al. 2013a, 2017a; Comerford et al. 2015), and integral-field spectroscopy (McGurk et al. 2011; Fu et al. 2012), in X-ray with *Chandra* (Comerford et al. 2011, 2015; Koss et al. 2011, 2012; Teng et al. 2012; Liu et al. 2013b; Ellison et al. 2017) and *NuStar* (Ptak et al. 2015; Koss et al. 2016), and in radio with the VLA (Fu et al. 2011b, 2015b; Müller-Sánchez et al. 2015) and the Very Long Baseline Array (Tingay & Wayth 2011; Deane et al. 2014; Wrobel et al. 2014; Bondi et al. 2016; Liu et al. 2017b). Identifying and confirming dAGN is a slow process; currently there are only a total of ~ 30

dAGN with projected separations less than 10 kpc in the literature (see Satyapal et al. 2017, for a compilation). Despite the small sample, there is now strong evidence that AGN activities are highly correlated in mergers while the AGN duty cycle remains more or less unchanged (e.g., Fu et al. 2018).

Observations at X-ray wavelengths can provide an effective measure of the accretion power of SMBHs in AGN. Nuclear X-ray emission in the keV-band could be produced by several mechanisms related to accretion: (1) inverse-Compton scattered thermal emission from a hot ($\sim 10^9$ K) corona (Liang & Price 1977; Haardt & Maraschi 1993) embedded in a cooler ($\sim 10^5$ K) standard geometrically thin optically thick disk (Shakura & Sunyaev 1973), (2) a hot ($\sim 10^{12}$ K at the Schwarzschild radius) advection-dominated accretion flow (ADAF; see Yuan & Narayan 2014, for a review), and (3) synchrotron and self-Comptonized emission from radiative shocks at the base of relativistic jets (Yuan et al. 2002). Although it is difficult to disentangle the contribution of the various mechanisms in individual AGN, generally speaking, the “disk-corona” model produces the “big blue bump” in the UV and soft X-ray and likely dominates at high Eddington ratios ($L_{\text{bol}}/L_{\text{Edd}} > 0.01$), while the “big blue bump” is absent in the ADAF and the “disk-jet” models, which dominate at low Eddington ratios ($L_{\text{bol}}/L_{\text{Edd}} < 0.01$). At low X-ray luminosity ($\lesssim 10^{42}$ erg s $^{-1}$), another complication arises: extended kiloparsec-scale emission may appear spatially unresolved at the *Chandra* resolution at $z \gtrsim 0.05$, where $1'' \gtrsim 1$ kpc. This makes it difficult to discern the X-ray emission due to the AGN central engine from emission of the surrounding host galaxy. Common nonnuclear X-ray emission from normal galaxies originates from (1) the hot ISM in hydrostatic equilibrium (often seen in early-type galaxies; e.g., Forman et al. 1985) and (2) X-ray binaries (XRBs), supernovae remnants, and hot winds produced by recent star formation (often seen in late-type galaxies and starburst galaxies; e.g., Fabbiano 1989). Such spatially extended sources of X-ray emission have typical luminosities between 10^{38} and 10^{42} erg s $^{-1}$, approaching the level of nuclear X-ray luminosity in Seyferts ($10^{42} < L_{0.5-10 \text{ keV}} < 10^{44}$ erg s $^{-1}$; Brusa et al. 2007).

Nuclear X-ray emission in the 0.5–10 keV band can be effectively absorbed by helium and heavier elements due to photoelectric absorption (Morrison & McCammon 1983). The obscuration can be caused by a dusty molecular torus at ~ 10 pc scales and the intervening ISM in the host galaxy. The former is suggested by the AGN unification scheme (Urry & Padovani 1995) and confirmed in observations of narrow-line FR II radio galaxies (e.g., Sambruna et al. 1999) and nearby Seyferts (e.g., Gallimore et al. 2016; García-Burillo et al. 2016; Alonso-Herrero et al. 2018; Fabbiano et al. 2018). But the torus may be absent at low accretion rates, such as in the FR I radio galaxies in the 3CR sample (e.g., Donato et al. 2004; Balmaverde et al. 2006; Evans et al. 2006) and the nearby low-luminosity AGN (LLAGN with $L_{0.5-10 \text{ keV}} < 10^{42}$ erg s $^{-1}$; see Ho 2008, for a review). In these cases, X-ray emission can only be obscured by the intervening ISM (e.g., Gilli et al. 2014). Because the gas column density is elevated during a galaxy merger by tidally induced gas inflows, one would expect an excess of obscured AGN in late-stage mergers (e.g., Hopkins et al. 2005).

In this series, we identify dAGN candidates within the 92 deg 2 covered by the wide-area 2''-resolution VLA 1.4 GHz survey of the Stripe 82 field (Fu et al. 2015a, hereafter Paper I).

Out of 17,969 discrete radio sources, we identify 52 candidate pairs, which show good positional alignments between the radio sources and their optical counterparts. Optical spectroscopy available for eight of these candidates at that time reveals six pairs with consistent redshifts. We then follow up on these candidates with 0''3-resolution VLA 6 GHz observations (Fu et al. 2015b, hereafter Paper II). The higher-resolution radio imaging reveals two of these candidate pairs to be projections of jets from single sources. The remaining four pairs are confirmed as dual AGN with compact ($\lesssim 0''4$) nuclear radio emission and core luminosities between $37.3 < \log L_{5 \text{ GHz}}/\text{erg s}^{-1} < 39.4$.

Here we present *Chandra* X-ray observations of this radio and optically confirmed sample of dual AGN. The X-ray data enable us to address two main questions: Do dAGN follow the same multiwavelength scaling relations as the general AGN population? Also, are dAGN obscured to a higher degree than the general AGN population? This paper is organized as follows. In Section 2 we describe the *Chandra* observations and data reduction procedures. In Section 3 we present the X-ray photometry and spectral fitting procedures. We synthesize our previous observations and the deduced X-ray properties of the dAGN in Section 4, wherein we test whether the dAGN deviate from the scaling relations established by general AGN of similar luminosities and also address whether dAGN are potentially more obscured at X-ray wavelengths. We conclude with a summary of our results and discuss their implications in Section 5. Throughout, we adopt a Λ CDM cosmology with $\Omega_{\text{m}} = 0.3$, $\Omega_{\Lambda} = 0.7$, and $h = 0.7$. As usual, the spectral index α and the photon index Γ are defined such that $F_{\nu} \propto \nu^{-\alpha}$ and $n(E) \propto E^{-\Gamma}$.

2. *Chandra* Observations

Our sample consists of four radio-selected kiloparsec-scale dAGN between $0.04 < z < 0.22$ in the SDSS Stripe 82 field (Paper II). All of the galactic nuclei show compact radio emission at a resolution of 0''3. The radio cores show projected separations between 2''6 and 4''7 (or 4.3 and 9.2 kpc). Under *Chandra* Cycle 18 Proposal # 18700044, we observed the targets with the Advanced CCD Imaging Spectrometer (ACIS) in 2016 October (Obs ID: 19456) and 2017 September (Obs IDs: 19453–19455). The targets were placed near the aim point on the back-illuminated S3 chip. The average integration time is 24 ks.

Data reduction and analysis is carried out with the *Chandra* Interactive Analysis of Observations software (CIAO v4.9; Fruscione et al. 2006). Because the first observation and the last observation took place almost a year apart, we reprocess all of the data to the calibration database (CALDB v4.7.7) with `chandra_repro`. We then focus on the data of the S3 chip (CCD ID: 7) in the calibrated energy range between 0.3 and 10 keV by filtering the calibrated level 2 event file with `dmcopy`. Only the events with grades 0, 2, 3, 4, and 6 were included. We detect no significant flares in the background light curves. In the observation of 2206+0003, the X-ray position of the southeast component of the dAGN (i.e., 2206+0003 SE) shows an offset of 0''26 from the VLA 6 GHz source. We correct for this astrometric offset in the ASOL file and the event-2 file with `wcs_update`. The other three observations show no significant astrometric offset wherever there are sufficient numbers of X-ray sources to carry out a positional comparison between the X-ray sources from

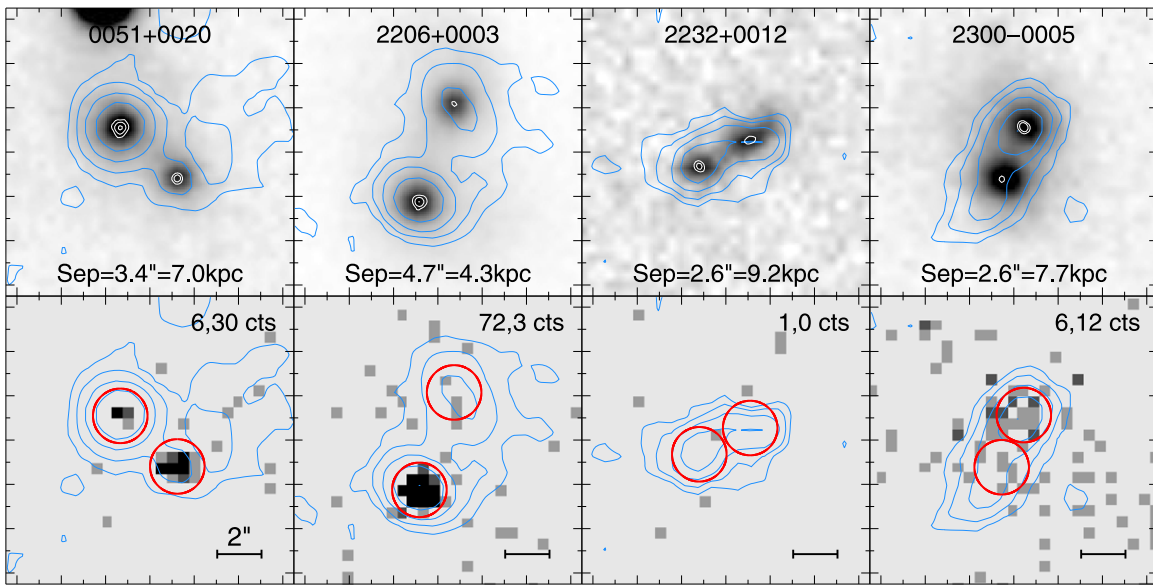


Figure 1. Near-IR and X-ray images of the dual AGN, with radio contours. For each system, we show: (top row) a UKIDSS H -band image overlaid with the VLA 6 GHz map (white contours; $0''.3$ beam) and the 1.4 GHz map from the VLA-Stripe 82 survey (blue contours; $1''.8$ beam), with the source short designation, and the projected separation of the 6 GHz radio cores; (bottom row) the ACIS image overlaid with the 1.4 GHz map, X-ray photometry apertures (red circles), the full-band X-ray counts for the east (left) and the west (right) components, and a $2''$ scale bar. The X-ray images are displayed in their native $\sim 0''.5$ pixels. The 6 GHz VLA contours are at $(+3, +6, +24, +96) \times \sigma$. The 1.4 GHz VLA contours start at 2σ and the levels increase exponentially to the peak S/N. Major tickmarks are spaced in $2''$ intervals. N is up and E is left for all panels.

wavdetect and the radio sources from our VLA observations and the near-IR sources from UKIRT IR Deep Sky Survey (UKIDSS; Warren et al. 2007).

Figure 1 shows the full-band (0.3–8 keV) X-ray images of the targets, along with their near-IR images, and radio maps. The first impression of the figure is that four of the eight nuclei are clearly detected (0051+0020 NE, 0051+0020 SW, 2206+0003 SE, and 2300–0005 NW), two are probably detected (2206+0003 NW and 2300–0005 SE), and two are clearly undetected (2232+0012 NW and 2232+0012 SE). We present more quantitative results from aperture photometry in the next section.

3. X-Ray Data Analysis

For source photometry, we adopt a 2.5 pixel-radius circular aperture centered at the VLA 6 GHz position (the native CCD pixel size of ACIS-S is $0''.4920$). This corresponds to aperture radii of 2.5, 1.1, 4.4, and 3.7 kpc for the sources in 0051+0020, 2206+0003, 2232+0012, and 2300–0005, respectively. The source aperture encloses 92%/88% of the point-spread function (PSF) at an effective energy of 1.5/3.6 keV from `arfcorr` and its diameter of $2''.46$ is slightly less than the angular separation of the most closely separated pair in our sample (thus avoiding aperture overlapping). The aperture is also large enough to fully enclose the 90% ACIS-S positional uncertainty radius of $\sim 0''.7$ (<http://cxc.harvard.edu/cal/ASPECT/celmon/>). To estimate the background contribution to the source counts, we define a background region using an annulus centered at the middle point of each pair with an inner and an outer radius of 20 pixels and 60 pixels, respectively. We exclude sources detected by `wavdetect` inside the background annulus with a 10 pixel radius circular region around each source. Counts from the source and background regions are measured with `srcflux` for three energy bands: soft (S ; 0.3–2 keV, $E_{\text{eff}} = 1.5$ keV), hard (H ; 2–8 keV, $E_{\text{eff}} = 4.3$ keV),

and full (F ; 0.3–8 keV, $E_{\text{eff}} = 3.6$ keV), where the effective energy (E_{eff}) is defined as the effective-area-weighted mean energy of each band. The full-band source counts range between 0 and 72, whereas the background is expected to contribute between 0.2 and 0.6 counts in the source aperture. The significance of the X-ray detections can be estimated using Poisson statistics. For the six AGN in 0051+0020, 2206+0003, and 2300–0005, the probability of the background counts constituting the observed counts in the aperture is less than 0.1% in the 0.3–8 keV band, which is equivalent to a confidence level of $>99.9\%$ for a detection of the source. We thus consider these six sources as robust detections. Both AGN in 2232+0012 are undetected, so we estimate the 3σ (99%) upper limits of the count rates using the background-marginalized Bayesian algorithm built into `aprates` and convert them to flux upper limits assuming an unabsorbed power-law model with $\Gamma = 1.9$, which is appropriate for AGN (e.g., Just et al. 2007; She et al. 2017). The statistical results are consistent with the visual impression of Figure 1. The total counts and the expected background counts in the three energy bands are listed in Table 1, along with a few derived parameters discussed below.

We estimate the hardness ratio, $\text{HR} \equiv (H-S)/(H+S)$, of the six detections using the Bayesian estimation method of Park et al. (2006). Assuming an intrinsic power-law spectrum with a fixed photon index, we can use the estimated HR to infer the intervening total hydrogen column density in the host galaxy (N_{H}). We again adopt the canonical power-law photon index of $\Gamma = 1.9$. For each target, we use the `modelflux` task to calculate the relation between HR and N_{H} for a redshifted power-law model with $\Gamma = 1.9$ absorbed intrinsically by the torus or the host galaxy and subsequently by $N_{\text{H}}^{\text{Gal}}$ from the Milky Way (`xszpowerlw * xszphabs * xsphabs`). The photoelectric absorption cross-sections (Balucinska-Church & McCammon 1992) assume the standard solar abundance set from Anders & Grevesse (1989). The $\text{HR}-N_{\text{H}}$ relation varies

Table 1
X-Ray Observations and Photometry

Object	z	Exptime (ks)	Full src (bkg)	Soft src (bkg)	Hard src (bkg)	HR	$\log N_{\text{H}}$ (cm^{-2})	$\log F_{0.3-8 \text{ keV}}^{\text{abs}}$ ($\text{erg s}^{-1} \text{cm}^{-2}$)	$\log F_{0.3-8 \text{ keV}}^{\text{unabs}}$ ($\text{erg s}^{-1} \text{cm}^{-2}$)
(1)	(2)	(3)	(4)	(5)	(6)	(7)	(8)	(9)	(10)
0051+0020 SW	0.11253	28.7	30 (0.3)	19 (0.1)	11 (0.2)	$-0.28^{+0.18}_{-0.17}$	$21.2^{+0.5}_{-1.2}$	$-13.9^{+0.1}_{-0.1}$	$-13.8^{+0.2}_{-0.2}$
0051+0020 NE	0.11257	28.7	6 (0.3)	3 (0.1)	3 (0.2)	$-0.02^{+0.40}_{-0.40}$	$21.9^{+0.5}_{-1.9}$	$-14.6^{+0.2}_{-0.2}$	$-14.3^{+0.4}_{-0.4}$
2206+0003 NW	0.04656	15.9	3 (0.2)	2 (0.1)	1 (0.1)	$-0.63^{+0.53}_{-0.26}$...	$-14.6^{+0.3}_{-0.3}$	$-14.6^{+0.3}_{-0.3}$
2206+0003 SE	0.04640	15.9	72(0.2)	7 (0.1)	65 (0.1)	$+0.82^{+0.06}_{-0.08}$	$22.7^{+0.1}_{-0.1}$	$-13.0^{+0.1}_{-0.1}$	$-12.4^{+0.1}_{-0.1}$
2232+0012 NW	0.22128	16.9	0 (0.2)	0 (0.1)	0 (0.1)	<-14.4	<-14.4
2232+0012 SE	0.22187	16.9	1 (0.2)	0 (0.1)	1 (0.1)	<-14.3	<-14.2
2300-0005 NW	0.17971	34.7	12 (0.6)	10 (0.3)	2 (0.3)	$-0.78^{+0.23}_{-0.17}$...	$-14.4^{+0.1}_{-0.1}$	$-14.3^{+0.1}_{-0.1}$
2300-0005 SE	0.17981	34.7	6 (0.6)	4 (0.3)	2 (0.3)	$-0.47^{+0.42}_{-0.35}$...	$-14.7^{+0.2}_{-0.2}$	$-14.7^{+0.2}_{-0.2}$

Note. Rows are grouped in sets of two that each include a pair, and sources are sorted in ascending R.A. (1) Object name; (2) spectroscopic redshift; (3) ACIS-S exposure time in kilosecond; (4–6) source and background counts inside a $2\frac{1}{2}$ diameter circular aperture centered on the radio position for full band (F , 0.3–8 keV), soft band (S , 0.3–2.0 keV), and hard band (H , 2.0–8.0 keV), respectively; (7) hardness ratio (HR) determined using Bayesian estimation method (BEHR; Park et al. 2006), which is defined as $\text{HR} = (H-S)/(H+S)$; quoted are the mode and the 15.8-and-84.1-percentiles; (8) intrinsic hydrogen column density inferred from HR by fixing the photon index at $\Gamma = 1.9$. Three of the six detected sources do not have N_{H} measurements because their nominal HRs are softer than the assumed power law; (9–10) absorbed and unabsorbed power-law model flux at the observed-frame full band. The absorbed flux includes both intrinsic absorption and Galactic absorption. Detections are quoted with the 1σ uncertainty, and nondetections are listed as upper limits at the 99% confidence level. The quoted error of the unabsorbed flux accounts for the uncertainties in both the count rate and the HR-derived intrinsic column density.

among the sources because of the differences in redshift, the Galactic column density ($N_{\text{H}}^{\text{Gal}}$), and the Auxiliary Response Function (ARF) and Redistribution Matrix Function (RMF) specific to the *Chandra* observation. The Galactic column densities from the NRAO catalog (Dickey & Lockman 1990) range between $2.66 \times 10^{20} \text{ cm}^{-2}$ and $5.21 \times 10^{20} \text{ cm}^{-2}$.

For three of the six detections (both sources in 0051+0020 and 2206+0003 SE) that have HRs greater than the unabsorbed power-law model (i.e., $\text{HR} > -0.4$), we can apply an HR-based method to self-consistently convert the count rate to absorbed and unabsorbed fluxes. We first use the HR– N_{H} -relation and the measured HR to estimate N_{H} , obtaining values for these three sources of $1.6 \times 10^{21} \text{ cm}^{-2} \lesssim N_{\text{H}} \lesssim 5 \times 10^{22} \text{ cm}^{-2}$. We then scale the PSF-corrected count rate to the absorbed and the unabsorbed flux in each energy band using the scaling factors from `modelflux` for the HR-derived N_{H} . The X-ray emission from these three sources appears spatially concentrated on the radio positions in Figure 1 (as expected for point sources) and their HRs are consistent with nuclear emission typically observed in AGN. Therefore, we conclude that the X-ray emission in 0051+0020 and 2206+0003 SE are powered by BH accretion and one of the three AGN are moderately obscured ($N_{\text{H}} > 10^{22} \text{ cm}^{-2}$). We note that although AGN are observed to have a range of photon indices, our choice of $\Gamma = 1.9$ does not significantly impact our results given the HR values for our sample. Varying the photon index by $\Delta\Gamma = 0.5$ in either direction yields $\Delta\log(N_{\text{H}}/\text{cm}^{-2}) = 0.4, 0.12, \text{ and } 0.07$ dex for $\text{HR} = 0, 0.5, \text{ and } 0.8$, respectively. The HRs of the other three detections (2206+0003 NW, and both sources in 2300–0005) are lower than the HR of an unabsorbed power-law model ($\text{HR} < -0.4$), so we calculate their fluxes assuming negligible intrinsic absorption.

Spectral fitting is only possible for 2206+0003 SE, which has 72 counts. We group the extracted spectrum to a minimum of five counts per bin and fit the grouped spectrum with the same absorbed power-law model using *Sherpa*. We assume

the same absorbed power-law model as above and allow Γ to vary between 1.4 and 2.4. We adopt Cash statistics because of the low counts. We find a best-fit column density of $\log(N_{\text{H}}/\text{cm}^{-2}) = 23.0 \pm 0.2$, which is consistent with the HR-derived value within 1.5 σ .

4. Results

Our *Chandra* observations provide the X-ray fluxes and the HRs of our dAGN, and for several cases, the column densities of the intervening gas (Table 1). To estimate the unabsorbed X-ray luminosity at rest-frame 2–10 keV ($L_{\text{X}} \equiv L_{2-10 \text{ keV}}$), we use the K -correction factor of the assumed power-law model to convert the unabsorbed 0.3–8 keV flux to the rest-frame flux in 2–10 keV. For the range of column densities observed in our sources ($N_{\text{H}} \leq 10^{23} \text{ cm}^{-2}$), the 2–10 keV luminosity is almost unaffected by absorption: photoelectric absorption by intervening gas with $N_{\text{H}} = 10^{23} \text{ cm}^{-2}$ only decreases the 2–10 keV luminosity by 0.28 dex. In Table 2, we list the X-ray luminosities of the dAGN along with their properties observed at other wavelengths.

In the following subsections, we perform a series of comparisons between the dAGN and the general AGN population to assess whether the dAGN behave differently. We begin in Section 4.1 by establishing the possible non-AGN sources of X-ray emission in our sample. We then compare the general AGN properties such as radio-to-X-ray ratio, Eddington ratio, and the BH fundamental plane in Section 4.2. In Section 4.3 we analyze the distribution of X-ray hardness ratios to test whether the AGN in mergers are more obscured than isolated AGN, as expected from tidally induced inflows. Finally, in Section 4.4 we check if the X-ray luminosities of dAGN are lower than expected from their mid-IR and [O III] luminosities and discuss the role of star formation in the dAGN.

Table 2
Multiwavelength Properties

Object	σ_* (km s^{-1})	$\log M_{\text{BH}}$ (M_{\odot})	$\log L_{\text{H}\alpha}$ (erg s^{-1})	$\log L_{[\text{O III}]}$ (erg s^{-1})	$\log L_{5 \text{ GHz}}$ (erg s^{-1})	$\log L_{12 \mu\text{m}}$ (erg s^{-1})	$\log L_X$ (erg s^{-1})	$\log L_X^{\text{XRB}}$ (erg s^{-1})
(1)	(2)	(3)	(4)	(5)	(6)	(7)	(8)	(9)
0051+0020 SW	140 ± 12	7.8 ± 0.3	41.80 ± 0.02	41.33 ± 0.11	38.73 ± 0.02	43.88 ± 0.02	$41.5^{+0.2}_{-0.2}$	40.0
0051+0020 NE	166 ± 9	8.1 ± 0.3	42.36 ± 0.01	41.37 ± 0.18	39.22 ± 0.01	...	$41.0^{+0.4}_{-0.4}$	40.4
2206+0003 NW	114 ± 9	7.4 ± 0.3	41.23 ± 0.01	40.63 ± 0.06	37.37 ± 0.10	42.77 ± 0.02	$39.9^{+0.3}_{-0.3}$	39.5
2206+0003 SE	170 ± 6	8.2 ± 0.3	41.55 ± 0.01	41.20 ± 0.03	38.22 ± 0.01	...	$42.0^{+0.1}_{-0.1}$	39.7
2232+0012 NW	244 ± 36	8.9 ± 0.4	41.18 ± 0.04	40.47 ± 0.08	39.03 ± 0.04	44.17 ± 0.02	<41.5	39.7
2232+0012 SE	210 ± 61	8.6 ± 0.6	41.51 ± 0.04	41.15 ± 0.08	39.28 ± 0.02	...	<41.7	39.9
2300–0005 NW	284 ± 13	9.2 ± 0.3	<40.50	<40.05	39.40 ± 0.01	43.28 ± 0.17	$41.4^{+0.1}_{-0.1}$	<40.4
2300–0005 SE	324 ± 11	9.4 ± 0.3	<40.62	<40.12	38.52 ± 0.09	...	$41.0^{+0.2}_{-0.2}$	<40.5

Note. (1) Object name; (2) stellar velocity dispersion from fitting SDSS and Keck/LRIS spectra with stellar population synthesis models (Paper II); (3) black hole mass inferred from the $M_{\text{BH}}-\sigma_*$ relation of Kormendy & Ho (2013), which has an intrinsic scatter of ~ 0.29 dex; (4–5) $\text{H}\alpha$ and [O III] $\lambda 5007$ line luminosities, corrected for reddening and aperture-loss; (6) rest-frame 5 GHz luminosity (νL_{ν}) computed from the VLA flux density at 6 GHz (Paper II); (7) rest-frame 12 μm luminosity from AllWISE photometry (listed is the total luminosity for each pair because the components are blended in WISE images); (8) unabsorbed rest-frame 2–10 keV luminosity K -corrected from the unabsorbed model flux ($F_{0.3-8 \text{ keV}}^{\text{unabs}}$) in Table 1; (9) expected X-ray luminosity from X-ray binaries.

4.1. Accounting for X-Ray Contamination

The AGN in our sample have unabsorbed rest-frame 2–10 keV luminosities in the range of $39.9 < \log L_X / \text{erg s}^{-1} < 42.0$, which is in the regime between nearby LLAGN and Seyferts (Brusa et al. 2007). In this regime, galactic sources of X-rays might be contributing significantly to the observed X-ray luminosity. Of particular concern is the contribution to L_X from XRBs, whose luminosity range can potentially overlap with LLAGN. Given the composite status and young stellar ages uncovered through BPT diagnostics in Paper I and spectral fitting in Paper II, respectively, the effects of XRBs should be taken into consideration. We first estimate the SFR using the extinction- and aperture-loss-corrected $\text{H}\alpha$ luminosities for our sample in the $L_{\text{H}\alpha}$ -SFR relation from Murphy et al. (2011):

$$\log(\text{SFR}/M_{\odot} \text{ yr}^{-1}) = \log(L_{\text{H}\alpha}^{\text{SF}}/\text{erg s}^{-1}) - 41.3. \quad (1)$$

These $\text{H}\alpha$ -based SFRs should be considered as upper limits because a significant fraction of the $\text{H}\alpha$ line may come from AGN-photoionized gas. We then use this expected SFR to calculate the expected L_X due to XRBs using the calibration from Lehmer et al. (2010):

$$L_X^{\text{XRB}} = \alpha \times M_* + \beta \times \text{SFR}, \quad (2)$$

where $\alpha = (9.05 \pm 0.37) \times 10^{28} \text{ (erg s}^{-1})/M_{\odot}$ and $\beta = (1.62 \pm 0.22) \times 10^{39} \text{ erg s}^{-1}/(M_{\odot} \text{ yr}^{-1})$. The first term traces the low-mass XRBs and the second term traces the high-mass XRBs. We use the stellar masses of the galaxies obtained through stellar population synthesis modeling in Paper II. We list the predicted values of L_X due to XRBs in Table 2. For seven of the eight sources, the observed L_X are more than ~ 0.6 dex above the predicted L_X from XRBs. For 2206+0003 NW, the difference is less than 0.4 dex, indicating significant contribution from XRBs. This is also consistent with the low HR (-0.63) of the source.

On the other hand, the low HRs of both sources in 2300–0005 is likely dominated by diffuse kiloparsec-scale thermal plasma with $T \sim 10^7 \text{ K}$ (i.e., $kT \sim 1 \text{ keV}$) in the host galaxies

(e.g., Donato et al. 2004). For reference, the intrinsic HR is about -0.8 for an *apec* thermal plasma model with $kT = 1 \text{ keV}$ and $Z = 0.2 Z_{\odot}$. Indeed, the X-ray emission of both sources appears spatially extended (e.g., simply compare 2300–0005 with 0051+0020 in Figure 1), although their counts are too low to allow a robust measurement of the radial profiles.

To sum up, we find that our sample consists of three sources (both objects in 0051+0020 and 2206+0003 SE) with definite AGN emission in X-ray, one source (2206+0003 NW) with nonnegligible contributions from XRBs, two sources (both objects in 2300–0005) with strong contributions from hot ISM, and two undetected sources (both objects in 2232+0012). For the latter five sources, the observed L_X should be considered as upper limits of the AGN X-ray luminosity.

4.2. General AGN Properties

We now compare the observed properties of our dAGN sample with those of AGN in isolated galaxies. In Figure 2, we plot R_X , the radio-to-X-ray luminosity ratio defined as $R_X \equiv \log(L_{5 \text{ GHz}}/L_X)$, against L_X . In this paper, the monochromatic radio luminosity is defined as νL_{ν} at rest-frame 5 GHz. To compare our dAGN with the general AGN populations, we show three comparison samples from the literature in Figure 2. First, in the low luminosity regime ($\log L_X \lesssim 42 \text{ erg s}^{-1}$), we adopt L_X from a sample of nearby ($< 50 \text{ Mpc}$) LLAGN from She et al. (2017) and cross-match the sources with the FIRST 1.4 GHz catalog (Helfand et al. 2015) to obtain the radio luminosity. Second, in the high luminosity regime ($\log L_X \gtrsim 42 \text{ erg s}^{-1}$), we plot the X-ray-selected AGN from the Stripe 82 X-ray Survey (LaMassa et al. 2016). Similar to the LLAGN sample, a K -correction was applied to the 1.4 GHz flux density assuming $\alpha = 0.7$. We also K -correct the observed luminosities in 0.5–7 keV (*Chandra*) and 0.5–10 keV (*XMM-Newton*) to rest-frame 2–10 keV assuming $\Gamma = 1.9$. Lastly, we include a subset of Palomar-Green (PG) QSOs, for which we compiled 5 GHz fluxes from Kellermann et al. (1989) and *XMM-Newton* X-ray luminosities from Piconcelli et al. (2005). The breadth of the parameter space covered by

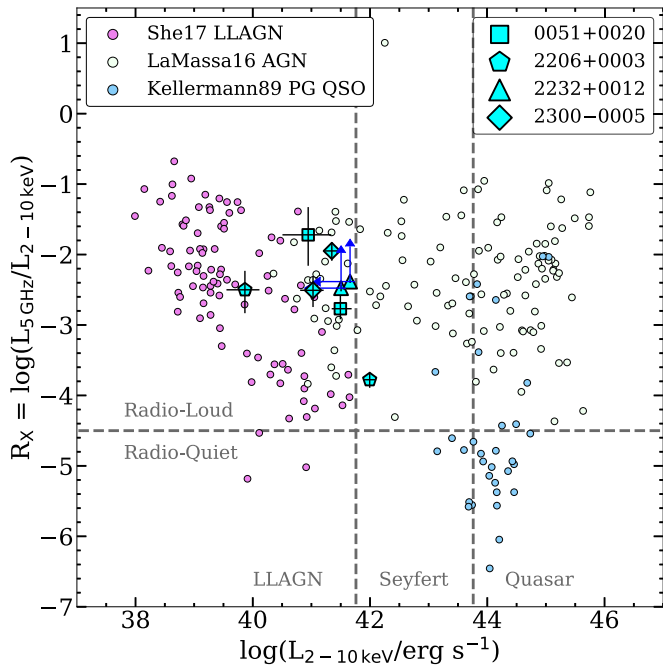


Figure 2. Radio-to-X-ray luminosity ratio (R_X) vs. unabsorbed rest-frame 2–10 keV luminosity (L_X). The cyan points show our sample, where a pair is denoted by the same shape. The small color-filled circles show the comparison samples described in Section 4.2 and are labeled in the legend on the upper left. Horizontal arrows indicate X-ray upper limits, and vertical arrows indicate lower limits in R_X . The vertical dashed lines at $\log(L_X/\text{erg s}^{-1}) = 41.76$ and 43.76 roughly divide AGN into three luminosity regimes: LLAGN, Seyfert, and Quasar (Brusa et al. 2007). The horizontal dashed line separates radio-loud ($R_X > -4.5$) and radio-quiet ($R_X < -4.5$) AGN. The dAGN have X-ray luminosities in the LLAGN regime and show similar radio-to-X-ray ratios.

these samples allows for a comprehensive comparison. This figure shows that the dAGN follow the same radio-X-ray scaling relation established by the general population of AGN, which are mostly hosted by isolated galaxies.

Note that even though we show a horizontal line at $R_X = -4.5$ to separate between radio-loud and radio-quiet AGN, R_X itself is not a robust indicator for accretion. In fact, star-forming galaxies have similar radio-to-X-ray ratios as the LLAGN in Figure 2. One obtains $R_X = -2.2$ for pure star-forming galaxies using the $L_{1.4\text{ GHz}}\text{-SFR}$ relation scaled to 5 GHz from Murphy et al. (2011) and the $L_X\text{-SFR}$ relation from Ranalli et al. (2003):

$$\log(L_X^{\text{SF}}/\text{erg s}^{-1}) = \log(\text{SFR}/M_\odot \text{ yr}^{-1}) + 39.7, \quad (3)$$

which constitutes an upper limit on the L_X from star formation related effects. On the other hand, R_X is directly related to the radio-to-X-ray spectral index between 5 GHz and 2 keV (4.84×10^{17} Hz):

$$\alpha_{\text{RX}} = (R_X + 8.242)/8 \quad \text{for } \Gamma = 1.9. \quad (4)$$

For the average value of $R_X = -2.5$ for our dAGN, α_{RX} equals 0.72, consistent with a single synchrotron spectrum extending from X-ray to radio (e.g., Hardcastle et al. 2001). Nonetheless, this crude SED slope measurement is inadequate to rule out models that predict separate origins of the X-ray and the radio emission.

The radio–X-ray correlation is closely related to the BH fundamental plane, which is established by both stellar-mass BHs in the Galaxy and the SMBHs in AGN and QSOs. The

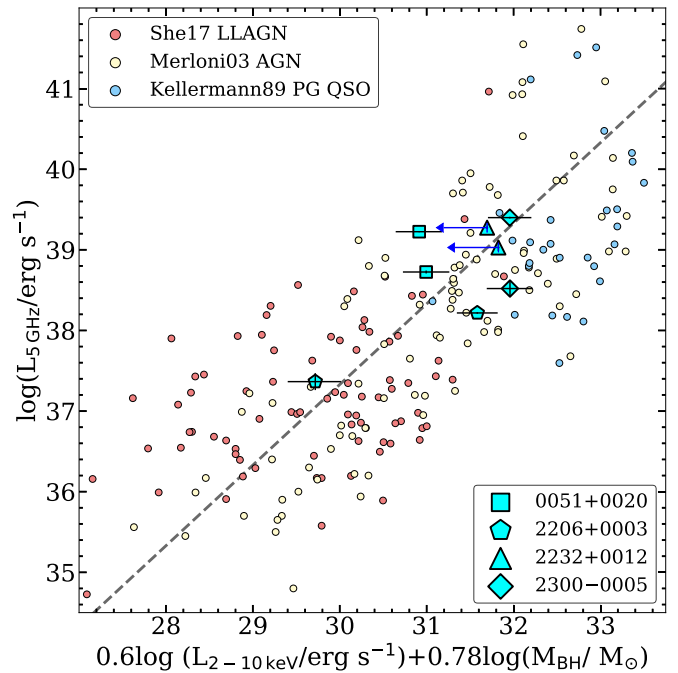


Figure 3. Black hole fundamental plane (Merloni et al. 2003). The dashed line follows the empirical relation given in Equation (5). The cyan points for our sample follow the same convention as in Figure 2. The arrows indicate X-ray upper limits. The smaller data points show the comparison samples described in Section 4.2. Our dAGN follow the fundamental plane relation with no systematic offsets well.

three-parameter empirical correlation is best-fit by the following power law (Merloni et al. 2003):

$$\begin{aligned} \log(L_{5\text{ GHz}}/\text{erg s}^{-1}) \\ = 0.6 \log(L_X/\text{erg s}^{-1}) + 0.78 \log(M_{\text{BH}}/M_\odot) + 7.33, \end{aligned} \quad (5)$$

where $L_{5\text{ GHz}}$, L_X , and M_{BH} are the rest-frame 5 GHz luminosity of the radio core, rest-frame 2–10 keV luminosity, and BH mass, respectively. Although the relation holds over an impressive range of BH mass and luminosity, it has a rather large scatter (~ 1 dex) and both the disk–jet model (Merloni et al. 2003) and the jet-dominated model (Falcke et al. 2004) can explain the same correlation.

With the X-ray luminosities from *Chandra* and the BH masses from the $M_{\text{BH}}\text{-}\sigma_*$ relation of nearby classical bulges and elliptical galaxies (Kormendy & Ho 2013), we can now place the dAGN on the fundamental plane in Figure 3. Similar to Figure 2, we also plot the following comparison samples: (1) the AGN from the original Merloni et al. (2003) sample, (2) LLAGN with *Chandra*/ACIS X-ray luminosity and BH mass from the $M_{\text{BH}}\text{-}\sigma_*$ relation (She et al. 2017) and 1.4 GHz radio flux from the FIRST survey (Helfand et al. 2015), and (3) PG QSOs with 5 GHz radio flux from Kellermann et al. (1989), *XMM-Newton* X-ray luminosity from Piconcelli et al. (2005), and $H\beta$ -based virial BH mass from Lani et al. (2017). It is clear from Figure 3 that the dAGN follow the same fundamental plane relation as the other AGN samples. They are distributed well within the scatter of the relation, with no systematic deviation from the best-fit relation.

Lastly, multiplying L_X by ~ 16 to estimate the bolometric luminosity (Ho 2008) and using the σ_* -derived BH mass to estimate the Eddington luminosity for ionized hydrogen, we

find that the dAGN have Eddington ratios between $-5 < \log L_{\text{bol}}/L_{\text{Edd}} < -3$, which again are similar to LLAGN. This last piece of evidence argues against a disk-corona model for the origin of nuclear X-rays in our dAGN.

In summary, we have compared the dAGN with other low-redshift AGN in terms of general AGN properties, such as radio-to-X-ray ratio, BH fundamental plane, and Eddington ratio. We find that the dAGN are similar to nearby LLAGN and Seyferts, suggesting that being involved in close galactic encounters does not affect these general AGN properties.

4.3. Distribution of X-Ray Hardness Ratios

Simulations suggest high gas column density in merging galaxies due to the central concentration of gas as the tidal torques funnel the ISM into the central kiloparsec (Hernquist 1989). The merger-driven model of quasars predicts a wide distribution of column densities ($N_{\text{H}} = 10^{21}\text{--}10^{25} \text{ cm}^{-2}$) with a peak around 10^{23} cm^{-2} (Hopkins et al. 2006). Our *Chandra* observations offer a way to test this prediction. As described in Section 3, we have obtained HR measurements for six sources in our dAGN sample. By assuming an unabsorbed photon index of the intrinsic AGN emission, the observed HRs can be used as a proxy for the column density, and we find that only one of the six sources is obscured (i.e., $N_{\text{H}} > 10^{22} \text{ cm}^{-2}$; see Table 1). In this subsection, we examine whether the distribution of the HR values is different from that of the general LLAGN.

To construct the control sample, we select 68 AGN with X-ray luminosities between $39.8 < \log L_{\text{X}}/\text{erg s}^{-1} < 42.0$ from the catalog of 314 nearby LLAGN observed by *Chandra* (She et al. 2017). The luminosity range matches that of the dAGN, so it prevents potential biases of the HRs due to any possible correlation between N_{H} and L_{X} . The control data set is an archival compilation obtained over many *Chandra* cycles, wherein the sensitivity of the detectors in soft X-ray is known to degrade over time due to increased contamination. Conversely, the effective area decreases for off-axis observations, and the effective area decreases faster in the hard energy band than the soft band. In addition, different detector arrays (ACIS-I versus ACIS-S) were used in the archival observations. For a fair comparison with the HR values of the dAGN, we institute correction factors to convert the reported HR values of the control sample to reflect the characteristics of ACIS-S in Cycle 18. Correction factors are computed utilizing the `modelflux` task with the ARF and RMF files of each source (kindly provided by Rui She), which encapsulate all of the above effects.

In Figure 4, we compare our dAGN sample and the control sample of LLAGN in the plane of X-ray luminosity versus HR. At first glance, the dAGN appear to be systematically softer X-ray sources than the control sample, contrary to the expectation that merger-driven inflows produce higher X-ray obscurations in the host galaxies, and thus higher HR values. Note that in the following comparison, we do not include either source in 2300–0005 or 2206+0003 NW, because their diffuse soft X-ray emission may originate from an interstellar thermal plasma or from XRBs, respectively, instead of nuclear accretion (Section 4.1). Between $39.8 < \log L_{\text{X}}/\text{erg s}^{-1} < 42.0$, 30 out of the 68 LLAGN in She et al. (2017) have $\text{HR} > 0.05$, which corresponds to $N_{\text{H}} > 10^{22} \text{ cm}^{-2}$ for $\Gamma = 1.9$. This fraction of obscured AGN is consistent with the previously determined distribution of

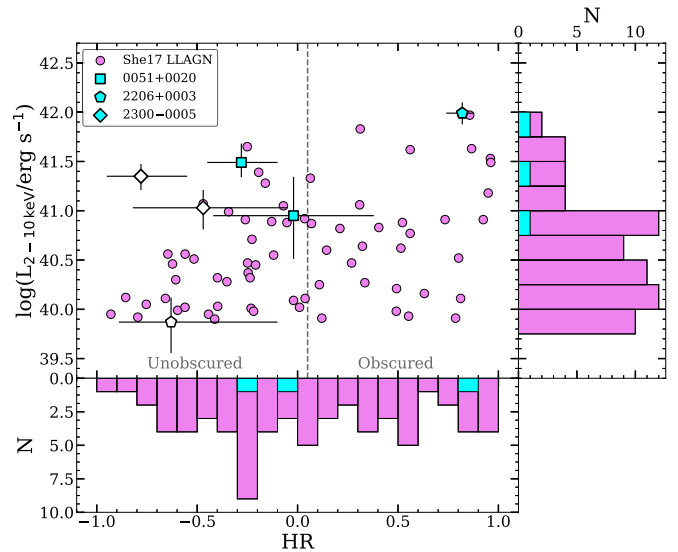


Figure 4. X-ray luminosity vs. hardness ratio. We show AGN-dominated components in our sample as filled shapes and histograms. Open shapes indicate the objects in our sample that have measured HR values, but are likely dominated by nonnuclear sources of soft X-ray emission as discussed in Section 4.1. We also show the control sample of nearby LLAGN from She et al. (2017; pink circles and histograms). The HR distribution of the dAGN is roughly consistent with that of the control sample. The vertical dashed line separates unobscured and obscured AGN.

column densities as a function of X-ray luminosity from Ueda et al. (2003). In contrast, only one out of the three dAGN components have $\text{HR} > 0.05$. Limited by the small sample size, the difference between the two obscured AGN fractions is within 1σ — $44 \pm 6\%$ versus $33^{+28}_{-15}\%$ —where the 1σ confidence intervals are estimated using the Bayesian approach for binomial population proportions (Cameron 2011). Therefore, the X-ray HRs of these dAGN are normal for their luminosity, lending no evidence that X-ray emission is more obscured in these galaxy mergers than in isolated AGN, even when the projected separations are less than 10 kpc. Given that only six of the individual components in our sample have measurable HR values, and three of these may be dominated by nonnuclear soft X-ray emission, a larger and deeper sample is needed to confirm this result.

4.4. Elevated Obscuration or Contamination from Star Formation?

Previous work argues that dAGN show higher degrees of obscuration by comparing the X-ray luminosity with the mid-IR ($12 \mu\text{m}$) luminosity (Satyapal et al. 2017). In this case, the observed X-ray luminosities of dAGN are lower than expected from the other AGN luminosity tracer. In this subsection, we apply the same diagnostic tools on the radio-selected dAGN and discuss their limitations.

In Figure 5 we plot X-ray luminosity against mid-IR luminosity, following Satyapal et al. (2017). For the dAGN, we interpolate the AllWISE photometry⁵ to obtain the rest-frame $12 \mu\text{m}$ luminosities ($L_{12 \mu\text{m}}$). Because our dAGN are spatially unresolved in *WISE* ($\text{FWHM} \sim 6''\text{--}12''$; Wright et al. 2010), the $12 \mu\text{m}$ luminosity is that of the whole dAGN system rather than that of individual components. To be consistent, we plot the combined X-ray luminosity for each dAGN. For

⁵ <http://wise2.ipac.caltech.edu/docs/release/allwise/expsup/>

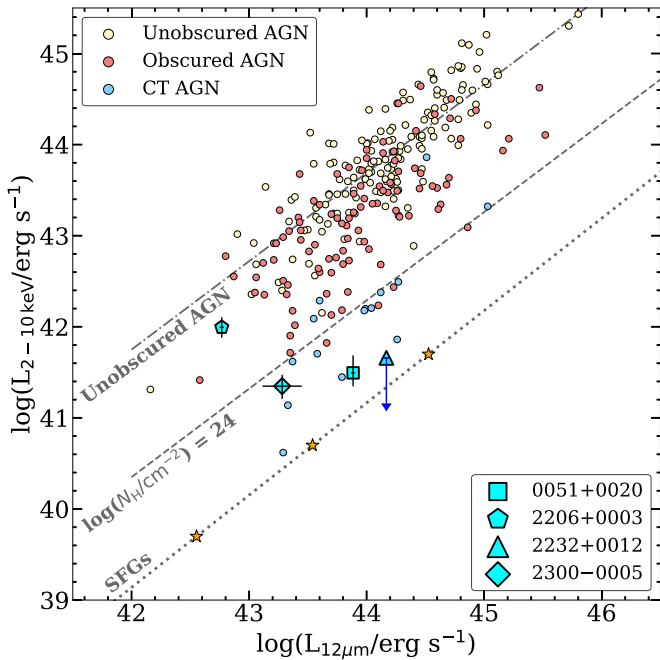


Figure 5. Luminosity relation sensitive to X-ray obscuration (L_X) vs. rest-frame $12\ \mu\text{m}$ luminosity from *WISE* ($L_{12\ \mu\text{m}}$). The large cyan data points with error bars show our dAGN and the small circles are BAT AGN from Ricci et al. (2015). The dotted-dashed line indicates the relation for the unobscured AGN in the comparison sample. The dashed line shows the predicted relation for AGN obscured by a column density of $N_H = 10^{24}\ \text{cm}^{-2}$ calculated by Satyapal et al. (2017) using a torus model that absorbs and reprocesses X-ray emission. Due to the spatial resolution of *WISE*, the luminosities plotted for the dAGN are the sum of both components in each dual system. The dotted line shows the expected relation for star-forming galaxies, with stars marking SFRs at 1, 10, and $100\ M_\odot\ \text{yr}^{-1}$. Arrows denote upper limits. The dAGN show apparent X-ray deficits relative to the mid-IR luminosities, which may be due to enhanced $L_{12\ \mu\text{m}}$ from star formation rather than elevated X-ray obscuration.

comparison with the general AGN population, we show the hard X-ray selected nearby AGN from the 70 month Swift/BAT survey (Baumgartner et al. 2013; Ricci et al. 2015). The BAT AGN are denoted as unobscured ($N_H < 10^{22}\ \text{cm}^{-2}$), obscured ($10^{22} < N_H < 10^{24}\ \text{cm}^{-2}$), or Compton-thick ($N_H > 10^{24}\ \text{cm}^{-2}$), based on column densities estimated from X-ray spectral analysis. As previously observed, unobscured BAT AGN follow a linear correlation between L_X and $L_{12\ \mu\text{m}}$, while obscured and Compton-thick AGN systematically deviate from this correlation by showing an apparent deficit in X-ray luminosity. This is because the mid-IR photons emitted by the circumnuclear torus are less affected by obscuration than the X-ray photons. This plot thus provides a diagnostic tool to identify obscured AGN, albeit crude given the large scatter around the best-fit correlation.

Similar to the previously X-ray observed dAGN compiled by Satyapal et al. (2017), the majority (3 out of 4) of the dAGN in our sample fall systematically below the $L_X-L_{12\ \mu\text{m}}$ correlation established by unobscured AGN and more closely resemble the Compton-thick AGN sample. Counterintuitively, the only obscured dAGN we identified based on the HR and the X-ray spectrum, 2206+0003, is in fact closest to the $L_X-L_{12\ \mu\text{m}}$ correlation. The apparent X-ray deficits for the remaining three dAGN imply high obscuring column densities. This is in tension with the low HR-derived column densities found in Section 3. To elucidate this matter, we show the expected location of star-forming galaxies as a dotted line in Figure 5, where we have used the $L_{12\ \mu\text{m}}-\text{SFR}$ relation from Donoso

et al. (2012):

$$\log(L_{12\ \mu\text{m}}^{\text{SF}}/\text{erg s}^{-1}) = 0.987 \log(\text{SFR}/M_\odot\ \text{yr}^{-1}) + 42.5, \quad (6)$$

as well as the $L_X-\text{SFR}$ relation given in Equation (3). Star-forming galaxies show a ~ 2.3 dex offset in L_X at any given $L_{12\ \mu\text{m}}$. So an alternative way to explain the location of the dAGN is that their mid-IR emission is dominated by star formation. While our dAGN do fall below the trend for unobscured AGN, the mid-IR contribution from star formation (in 0051+0020, 2206+0003, and 2232+0012, which are classified as star-forming/AGN composites on the BPT diagram) and stars in the host galaxies (in 2300-0005, which has no active star formation) may offer alternative interpretations for the observed offsets other than elevated X-ray obscuration. There is a caveat to this approach for sources with significant nonnuclear soft X-ray emission (Section 4.1). The observed HR of the source may artificially appear lower, potentially masking the absorbed signature of a highly obscured LLAGN.

To assess whether our sources are dominated by AGN or star formation in the near-IR, we check their *WISE* W1 ($3.4\ \mu\text{m}$) – W2 ($4.6\ \mu\text{m}$) colors provided by Satyapal et al. (2017). Two of our dual systems are identified as AGN by *WISE* using a generous threshold of $W1 - W2 > 0.5$ (0051+0020 and 2232+0012). Assuming that the mid-IR contribution from star formation is unimportant in *WISE*-color-selected AGNs, the results in Figure 5 would indicate that the AGN X-ray emission in 0051+0020 and 2232+0012 are heavily obscured. This seems inconsistent with the soft X-ray HRs observed in 0051+0020, especially considering that XRBs are insignificant in this system (Section 4.1). Unfortunately, to check the level of obscuration in 2232+0012, we would need much deeper X-ray observations.

The $[\text{O III}]\lambda 5007$ line emission from the kiloparsec-scale extended AGN narrow-line region is less affected by nuclear obscuration than the nuclear X-ray emission. This makes the $L_X-L_{[\text{O III}]}$ ratio another diagnostic tool for obscuration similar to the $L_X-L_{12\ \mu\text{m}}$ diagnostic (Panessa et al. 2006). Liu et al. (2013b) found that the X-ray to $[\text{O III}]$ luminosity ratios of double-peaked $[\text{O III}]$ -selected dAGN are systematically lower than those of optically selected single type 2 AGN. They suggest that the dAGN are systematically X-ray weak because of higher X-ray absorption columns and/or viewing angle bias from the double-peaked selection. We test whether a similar X-ray deficit is present in our sample of dAGN using the optical spectroscopy from Paper II. Comparing to the observed $L_X-L_{[\text{O III}]}$ relation established by isolated AGN (Panessa et al. 2006; Trichas et al. 2013), our sample of dAGN show an average offset of ~ 1.2 dex in L_X , suggesting higher levels of obscuration than the HR-derived column densities. When considering only the three AGN-dominated components, the average offset is ~ 1.5 dex, in comparison to the double-peaked $[\text{O III}]$ -selected sample of dAGN presented in Liu et al. (2013a), which have an average X-ray deficiency of ~ 2.5 dex. Furthermore, the large scatter in the control sample of isolated AGN used to establish the observed $L_X-L_{[\text{O III}]}$ relation encompasses the majority of our sample. So our radio-selected dAGN appear to be systematically less X-ray-weak than the double-peaked $[\text{O III}]$ -selected dAGN. As with the $L_X-L_{12\ \mu\text{m}}$ comparison above, the contribution to the observed $L_{[\text{O III}]}$ from star formation may also explain the apparent offset as an

enhancement of the [O III] luminosity as opposed to an X-ray deficiency from enhanced obscuration. As above, the caveat for artificially low HR values applies to the sources in our sample with contamination from nonnuclear soft X-rays.

5. Summary and Conclusion

In this work, we have obtained *Chandra* ACIS-S observations of four kiloparsec-scale radio-selected dAGN in Stripe 82. We detect X-ray emission from six of the eight dAGN components at $>3\sigma$ confidence level. Three X-ray components are consistent with low luminosity AGN. We find evidence for significant nonnuclear X-ray activity for the remaining three detected components. The X-ray and multiwavelength properties of the dAGN are analyzed and compared with general AGN populations and previously studied dAGN. Our main results are summarized below:

1. The intrinsic rest-frame 2–10 keV luminosities of our sample ranges between $39.9 < \log L_X/\text{erg s}^{-1} < 42.0$, straddling the luminosity boundary between nearby LLAGN and Seyferts. With $7.4 < \log M_{\text{BH}}/M_\odot < 9.4$ and $37.4 < \log L_{5\text{ GHz}}/\text{erg s}^{-1} < 39.4$, the components in the dAGN show low Eddington ratios and high radio-to-X-ray luminosity ratios similar to those of LLAGN, and they follow the same BH fundamental plane relation as the general AGN population.
2. The X-ray hardness ratios indicate one obscured AGN (with $\log N_{\text{H}}/\text{cm}^{-2} = 22.7$) among the three AGN-dominated X-ray sources. X-ray spectral fitting of this source finds a similarly high column density. The fraction of obscured AGN ($33^{+28}_{-15}\%$) is comparable to that of nearby LLAGN in the same luminosity range ($44 \pm 6\%$). This result is at odds with simulation predictions of enhanced obscuration in advanced mergers due to large-scale gas inflows.
3. The dAGN show apparent X-ray deficiency with respect to the AGN luminosities inferred from the $12\ \mu\text{m}$ *WISE* photometry and the [O III] spectroscopy, similar to previously studied dAGN selected using other techniques. But it is important to account for the contribution from star formation when interpreting the “X-ray deficit,” because the AGN luminosities inferred from mid-IR continuum and optical emission lines may have been significantly overestimated without subtracting the non-AGN components.

Considering the multiwavelength evidence, the radio-selected dAGN in Stripe 82 show properties similar to nearby LLAGN in terms of radio-to-X-ray ratio, the Eddington ratio, and BH mass. Although apparent X-ray deficiency is observed relative to mid-IR or [O III] luminosities in the dAGN, significant contribution to $L_{12\ \mu\text{m}}$ and $L_{[\text{O III}]}$ from star formation (i.e., mid-IR and emission-line excess) provides a more natural explanation for the data. This alternative interpretation is also more consistent with (1) the agreement with the BH fundamental plane (Section 4.2), (2) the normal X-ray HR distribution (Section 4.3), and (3) the AGN–star-forming composite emission-line ratios in the BPT diagram (see Paper I, Figure 6).

Despite our small sample, we find that these radio-selected dAGN show that being involved in close galactic encounters does not measurably alter their general AGN properties, nor does it increase their observed X-ray obscuring column density.

These results seem to be in tension with the merger-driven scenario of AGN fueling, especially given that (1) these galaxies are in kiloparsec-scale mergers, (2) at least two of the dAGN show spectacular tidal tails and shells that indicate a post-pericentric encounter, and (3) the number of observed dAGN exceeds by an order of magnitude the expectation from random pairing and the mean duty cycle of radio AGN in VLA-Stripe 82 (3 observed versus 0.3 expected ($13 \times (551/22192)$); see Paper II, Section 3.4).

To reconcile these results, the most promising feeding mechanism to explain the low-level AGN activities in our dAGN seems to be stochastic-mode accretion due to tidally triggered minor perturbations (e.g., Hopkins & Hernquist 2006). In contrast to the conventional “merger-driven accretion” where the SMBH accretion is fueled by kiloparsec-scale gas inflows and regulated by feedback (e.g., Di Matteo et al. 2005; Hopkins et al. 2005), the stochastic accretion naturally explains the similarities between the dAGN and LLAGN in apparently noninteracting hosts and the high frequency of correlated AGN (thus the higher-than-expected number of dAGN), but it evades the problem of enhanced obscuring column density due to large-scale tidal inflows (which is unobserved in our sample). Because an LLAGN with $L_{\text{bol}} \lesssim 10^{10} L_\odot$ and a lifetime of 10 Myr only requires a modest gas supply ($M \lesssim 6 \times 10^4 / (\eta_{\text{rad}}/0.1) M_\odot$, where η_{rad} is the radiative efficiency), large-scale gravitational torques from major mergers are not required to deliver the gas to the galactic nuclei. Instead, a sufficient amount of gas can be delivered to the nuclei even by a low-level cooling flow of the hot ISM (e.g., Allen et al. 2006), and minor perturbations such as disk and bar instabilities (e.g., Norman & Silk 1983; Jogee 2006), magnetic breaking (e.g., Krolik & Meiksin 1990), *N*-body cloud–cloud or cloud–cluster interactions like in the Galactic center (e.g., Genzel et al. 1994), and minor mergers (e.g., Hernquist & Mihos 1995). Once the nuclear gas reservoir has been built up, the black hole can accrete gas through stochastic cloud collisions, and the accretion is subsequently self-regulated by feedback (e.g., Yuan & Li 2011; Bu & Yang 2019). This stochastic accretion mode is distinct from the major-merger-induced accretion mode, and the former dominates the latter in the AGN population below the Seyfert/Quasar transition luminosity of $L_{\text{bol}} = 10^{12} L_\odot$ (Hopkins et al. 2014). The low-level AGN in major mergers in our sample suggest that the stochastic mode has continued to operate in these systems even in the presence of large-scale tidal torques. The gas-rich major mergers may not have induced kiloparsec-scale gas inflows (which would have obscured the X-ray), but they may have triggered minor perturbations in both nuclei simultaneously, which led to the high fraction of correlated LLAGN in mergers. This scenario represents a hybrid between the two above scenarios, namely merger-assisted stochastic accretion. This confluence of triggering mechanisms may be at play in some of the previously identified low luminosity dAGN systems as well (e.g., Liu et al. 2013b; Comerford et al. 2015; Fu et al. 2018).

We thank the anonymous referee for thoughtful comments that helped improve the paper. We thank Philip Kaaret, Cornelia Lang, Joshua Steffen, and Dylan Paré for helpful discussions, and Hua Feng, Claudio Ricci, Shobita Satyapal, and Rui She for providing data from their previous analyses. The scientific results reported in this article are based on observations made by the *Chandra* X-ray Observatory. Support

for this work was provided by the National Aeronautics and Space Administration (NASA) through Chandra Award Number GO7-18084X issued by the Chandra X-ray Center, which is operated by the Smithsonian Astrophysical Observatory for and on behalf of the National Aeronautics Space Administration under contract NAS8-03060. A.G. and H.F. acknowledge support from the National Science Foundation (NSF) grant AST-1614326. A.D.M. acknowledges support from NSF grant AST-1616168. S.G.D. acknowledges support from NSF grants AST-1413600 and AST-1518308, as well as NASA grant 16-ADAP16-0232. This research has made use of software provided by the Chandra X-ray Center (CXC) in the application packages CIAO, ChIPS, and Sherpa.

ORCID iDs

Arran C. Gross  <https://orcid.org/0000-0001-7681-9213>
 Hai Fu  <https://orcid.org/0000-0001-9608-6395>
 J. M. Wrobel  <https://orcid.org/0000-0001-9720-7398>
 S. G. Djorgovski  <https://orcid.org/0000-0002-0603-3087>

References

- Allen, S. W., Dunn, R. J. H., Fabian, A. C., Taylor, G. B., & Reynolds, C. S. 2006, *MNRAS*, **372**, 21
- Alonso-Herrero, A., Pereira-Santaella, M., García-Burillo, S., et al. 2018, *ApJ*, **859**, 144
- Anders, E., & Grevesse, N. 1989, *GeCoA*, **53**, 197
- Ballo, L., Braito, V., Della Ceca, R., et al. 2004, *ApJ*, **600**, 634
- Balmaverde, B., Capetti, A., & Grandi, P. 2006, *A&A*, **451**, 35
- Balucinska-Church, M., & McCammon, D. 1992, *ApJ*, **400**, 699
- Barnes, J. E., & Hernquist, L. E. 1991, *ApJL*, **370**, L65
- Baumgartner, W. H., Tueller, J., Markwardt, C. B., et al. 2013, *ApJS*, **207**, 19
- Bianchi, S., Chiaberge, M., Piconcelli, E., Guainazzi, M., & Matt, G. 2008, *MNRAS*, **386**, 105
- Blecha, L., Civano, F., Elvis, M., & Loeb, A. 2013, *MNRAS*, **428**, 1341
- Bondi, M., Pérez-Torres, M. A., Piconcelli, E., & Fu, H. 2016, *A&A*, **588**, A102
- Brassington, N. J., Ponman, T. J., & Read, A. M. 2007, *MNRAS*, **377**, 1439
- Brusa, M., Zamorani, G., Comastri, A., et al. 2007, *ApJS*, **172**, 353
- Bu, D.-F., & Yang, X.-H. 2019, arXiv:1901.00972
- Cameron, E. 2011, *PASA*, **28**, 128
- Capelo, P. R., & Dotti, M. 2017, *MNRAS*, **465**, 2643
- Comerford, J. M., Gerke, B. F., Newman, J. A., et al. 2009, *ApJ*, **698**, 956
- Comerford, J. M., Pooley, D., Barrows, R. S., et al. 2015, *ApJ*, **806**, 219
- Comerford, J. M., Pooley, D., Gerke, B. F., & Madejski, G. M. 2011, *ApJL*, **737**, L19
- Deane, R. P., Paragi, Z., Jarvis, M. J., et al. 2014, *Natur*, **511**, 57
- Dickey, J. M., & Lockman, F. J. 1990, *ARA&A*, **28**, 215
- Di Matteo, T., Springel, V., & Hernquist, L. 2005, *Natur*, **433**, 604
- Donato, D., Sambruna, R. M., & Gliozzi, M. 2004, *ApJ*, **617**, 915
- Donoso, E., Yan, L., Tsai, C., et al. 2012, *ApJ*, **748**, 80
- Ellison, S. L., Patton, D. R., Mendel, J. T., & Scudder, J. M. 2011, *MNRAS*, **418**, 2043
- Ellison, S. L., Secrest, N. J., Mendel, J. T., Satyapal, S., & Simard, L. 2017, *MNRAS*, **470**, L49
- Evans, D. A., Worrall, D. M., Hardcastle, M. J., Kraft, R. P., & Birkinshaw, M. 2006, *ApJ*, **642**, 96
- Fabbiano, G. 1989, *ARA&A*, **27**, 87
- Fabbiano, G., Paggi, A., Siemiginowska, A., & Elvis, M. 2018, arXiv:1812.02764
- Fabbiano, G., Wang, J., Elvis, M., & Risaliti, G. 2011, *Natur*, **477**, 431
- Falcke, H., Körding, E., & Markoff, S. 2004, *A&A*, **414**, 895
- Forman, W., Jones, C., & Tucker, W. 1985, *ApJ*, **293**, 102
- Fruscione, A., McDowell, J. C., Allen, G. E., et al. 2006, *Proc. SPIE*, **6270**, 62701V
- Fu, H., Myers, A. D., Djorgovski, S. G., et al. 2015a, *ApJ*, **799**, 72
- Fu, H., Myers, A. D., Djorgovski, S. G., & Yan, L. 2011a, *ApJ*, **733**, 103
- Fu, H., Steffen, J. L., Gross, A. C., et al. 2018, *ApJ*, **856**, 93
- Fu, H., Wrobel, J. M., Myers, A. D., Djorgovski, S. G., & Yan, L. 2015b, *ApJL*, **815**, L6
- Fu, H., Yan, L., Myers, A. D., et al. 2012, *ApJ*, **745**, 67
- Fu, H., Zhang, Z.-Y., Assef, R. J., et al. 2011b, *ApJL*, **740**, L44
- Gallimore, J. F., Elitzur, M., Maiolino, R., et al. 2016, *ApJL*, **829**, L7
- García-Burillo, S., Combes, F., Ramos Almeida, C., et al. 2016, *ApJL*, **823**, L12
- Genzel, R., Hollenbach, D., & Townes, C. H. 1994, *RPPh*, **57**, 417
- Gerke, B. F., Newman, J. A., Lotz, J., et al. 2007, *ApJL*, **660**, L23
- Gilli, R., Norman, C., Vignali, C., et al. 2014, *A&A*, **562**, A67
- Haardt, F., & Maraschi, L. 1993, *ApJ*, **413**, 507
- Hardcastle, M. J., Birkinshaw, M., & Worrall, D. M. 2001, *MNRAS*, **326**, 1499
- Helfand, D. J., White, R. L., & Becker, R. H. 2015, *ApJ*, **801**, 26
- Hernquist, L. 1989, *Natur*, **340**, 687
- Hernquist, L., & Mihos, J. C. 1995, *ApJ*, **448**, 41
- Ho, L. C. 2008, *ARA&A*, **46**, 475
- Hopkins, P. F., & Hernquist, L. 2006, *ApJS*, **166**, 1
- Hopkins, P. F., Hernquist, L., Cox, T. J., et al. 2006, *ApJS*, **163**, 1
- Hopkins, P. F., Hernquist, L., Martini, P., et al. 2005, *ApJL*, **625**, L71
- Hopkins, P. F., Kocevski, D. D., & Bundy, K. 2014, *MNRAS*, **445**, 823
- Jogee, S. 2006, in *Physics of Active Galactic Nuclei at all Scales*, Vol. 693, ed. D. Alloin (Berlin: Springer), 143
- Junkkarinen, V., Shields, G. A., Beaver, E. A., et al. 2001, *ApJL*, **549**, L155
- Just, D. W., Brandt, W. N., Shemmer, O., et al. 2007, *ApJ*, **665**, 1004
- Kellermann, K. I., Sramek, R., Schmidt, M., Shaffer, D. B., & Green, R. 1989, *AJ*, **98**, 1195
- Komossa, S., Burwitz, V., Hasinger, G., et al. 2003, *ApJL*, **582**, L15
- Kormendy, J., & Ho, L. C. 2013, *ARA&A*, **51**, 511
- Koss, M., Mushotzky, R., Treister, E., et al. 2011, *ApJL*, **735**, L42
- Koss, M., Mushotzky, R., Treister, E., et al. 2012, *ApJL*, **746**, L22
- Koss, M., Mushotzky, R., Veilleux, S., & Winter, L. 2010, *ApJL*, **716**, L125
- Koss, M. J., Glidden, A., Baloković, M., et al. 2016, *ApJL*, **824**, L4
- Krolik, J. H., & Meiksin, A. 1990, *ApJL*, **352**, L33
- LaMassa, S. M., Urry, C. M., Cappelluti, N., et al. 2016, *ApJ*, **817**, 172
- Lani, C., Netzer, H., & Lutz, D. 2017, *MNRAS*, **471**, 59
- Lehmer, B. D., Alexander, D. M., Bauer, F. E., et al. 2010, *ApJ*, **724**, 559
- Liang, E. P. T., & Price, R. H. 1977, *ApJ*, **218**, 247
- Liu, J.-F., Bregman, J. N., Bai, Y., Justham, S., & Crowther, P. 2013a, *Natur*, **503**, 500
- Liu, X., Civano, F., Shen, Y., et al. 2013b, *ApJ*, **762**, 110
- Liu, X., Guo, H., Shen, Y., Greene, J. E., & Strauss, M. A. 2017a, arXiv:1712.01866
- Liu, X., Lazio, T. J. W., Shen, Y., & Strauss, M. A. 2017b, arXiv:1709.03561
- Liu, X., Shen, Y., & Strauss, M. A. 2012, *ApJ*, **745**, 94
- Liu, X., Shen, Y., Strauss, M. A., & Greene, J. E. 2010, *ApJ*, **708**, 427
- Mazzarella, J. M., Iwasawa, K., Vavilkin, T., et al. 2012, *AJ*, **144**, 125
- McGurk, R. C., Max, C. E., Rosario, D. J., et al. 2011, *ApJL*, **738**, L2
- Merloni, A., Heinz, S., & di Matteo, T. 2003, *MNRAS*, **345**, 1057
- Morrison, R., & McCammon, D. 1983, *ApJ*, **270**, 119
- Müller-Sánchez, F., Comerford, J. M., Nevin, R., et al. 2015, *ApJ*, **813**, 103
- Murphy, E. J., Condon, J. J., Schinnerer, E., et al. 2011, *ApJ*, **737**, 67
- Norman, C., & Silk, J. 1983, *ApJ*, **266**, 502
- Owen, F. N., O’Dea, C. P., Inoue, M., & Eilek, J. A. 1985, *ApJL*, **294**, L85
- Panessa, F., Bassani, L., Cappi, M., et al. 2006, *A&A*, **455**, 173
- Park, T., Kashyap, V. L., Siemiginowska, A., et al. 2006, *ApJ*, **652**, 610
- Piconcelli, E., Jimenez-Bailón, E., Guainazzi, M., et al. 2005, *A&A*, **432**, 15
- Pillepich, A., Nelson, D., Hernquist, L., et al. 2018, *MNRAS*, **475**, 648
- Ptak, A., Hornschemeier, A., Zezas, A., et al. 2015, *ApJ*, **800**, 104
- Ranalli, P., Comastri, A., & Setti, G. 2003, *A&A*, **399**, 39
- Ricci, C., Ueda, Y., Koss, M. J., et al. 2015, *ApJL*, **815**, L13
- Rodríguez-Gomez, V., Pillepich, A., Sales, L. V., et al. 2016, *MNRAS*, **458**, 2371
- Rosario, D. J., McGurk, R. C., Max, C. E., et al. 2011, *ApJ*, **739**, 44
- Rosas-Guevara, Y., Bower, R., McAlpine, S., Bonoli, S., & Tissera, P. 2018, arXiv:1805.01479
- Sambruna, R. M., Eracleous, M., & Mushotzky, R. F. 1999, *ApJ*, **526**, 60
- Satyapal, S., Ellison, S. L., McAlpine, W., et al. 2014, *MNRAS*, **441**, 1297
- Satyapal, S., Secrest, N. J., Ricci, C., et al. 2017, *ApJ*, **848**, 126
- Shakura, N. I., & Sunyaev, R. A. 1973, *A&A*, **24**, 337
- She, R., Ho, L. C., & Feng, H. 2017, *ApJ*, **835**, 223
- Smith, K. L., Shields, G. A., Bonning, E. W., et al. 2010, *ApJ*, **716**, 866
- Stockton, A., Canalizo, G., Nelan, E. P., & Ridgway, S. E. 2004, *ApJ*, **600**, 626
- Teng, S. H., Schawinski, K., Urry, C. M., et al. 2012, *ApJ*, **753**, 165
- Tingay, S. J., & Wayth, R. B. 2011, *AJ*, **141**, 174
- Torrey, P., Vogelsberger, M., Sijacki, D., Springel, V., & Hernquist, L. 2012, *MNRAS*, **427**, 2224
- Trichas, M., Green, P. J., Constantin, A., et al. 2013, *ApJ*, **778**, 188
- Ueda, Y., Akiyama, M., Ohta, K., & Miyaji, T. 2003, *ApJ*, **598**, 886
- Urry, C. M., & Padovani, P. 1995, *PASP*, **107**, 803

Van Wassenhove, S., Volonteri, M., Mayer, L., et al. 2012, [ApJL](#), **748**, L7
Wang, J.-M., Chen, Y.-M., Hu, C., et al. 2009, [ApJL](#), **705**, L76
Warren, S. J., Hambly, N. C., Dye, S., et al. 2007, [MNRAS](#), **375**, 213
Wright, E. L., Eisenhardt, P. R. M., Mainzer, A. K., et al. 2010, [AJ](#), **140**, 1868

Wrobel, J. M., Walker, R. C., & Fu, H. 2014, [ApJL](#), **792**, L8
Yuan, F., & Li, M. 2011, [ApJ](#), **737**, 23
Yuan, F., Markoff, S., Falcke, H., & Biermann, P. L. 2002, [A&A](#), **391**, 139
Yuan, F., & Narayan, R. 2014, [ARA&A](#), **52**, 529